




Cite this: *Nanoscale*, 2024, **16**, 10428

NIR and magnetism dual-response multi-core magnetic vortex nanoflowers for boosting magneto-photothermal cancer therapy†

Kaiming Shen,^a Lixian Li,^{*b} Funan Tan,^c Calvin Ching Ian Ang,^c Tianli Jin,^c Zongguo Xue,^a Shuo Wu,^c Mun Yin Chee,^c Yunfei Yan ^{*a} and Wen Siang Lew^{*c}

Due to the relatively low efficiency of magnetic hyperthermia and photothermal conversion, it is rather challenging for magneto-photothermal nanoagents to be used as an effective treatment during tumor hyperthermal therapy. The advancement of magnetic nanoparticles exhibiting a vortex-domain structure holds great promise as a viable strategy to enhance the application performance of conventional magnetic nanoparticles while retaining their inherent biocompatibility. Here, we report the development of $\text{Mn}_{0.5}\text{Zn}_{0.5}\text{Fe}_2\text{O}_4$ nanoflowers with ellipsoidal magnetic cores, and show them as effective nanoagents for magneto-photothermal synergistic therapy. Comparative studies were conducted on the heating performance of anisometric $\text{Mn}_{0.5}\text{Zn}_{0.5}\text{Fe}_2\text{O}_4$ (MZF) nanoparticles, including nanocubes (MZF-C), hollow spheres (MZF-HS), nanoflowers consisting of ellipsoidal magnetic cores (MZF-NFE), and nanoflowers consisting of needle-like magnetic cores (MZF-NFN). MZF-NFE exhibits an intrinsic loss parameter (ILP) of up to $15.3 \text{ N h m}^2 \text{ kg}^{-1}$, which is better than that of commercial equivalents. Micromagnetic simulations reveal the magnetization configurations and reversal characteristics of the various MZF shapes. Additionally, all nanostructures displayed a considerable photothermal conversion efficiency rate of more than 18%. Our results demonstrated that by combining the dual exposure of MHT and PTT for hyperthermia treatments induced by MZF-NFE, BT549, MCF-7, and 4T1 cell viability can be significantly decreased by $\sim 95.7\%$ *in vitro*.

Received 9th January 2024,

Accepted 28th April 2024

DOI: 10.1039/d4nr00104d

rsc.li/nanoscale

Introduction

Magnetic hyperthermia emerges as a highly promising medical treatment approach, harnessing the heat generated by magnetic nanoparticles (MNPs) upon exposure to an applied alternating magnetic field (AMF), effectively targeting and eradicating tumor cells.^{1–5} There are several advantages of mag-

netic hyperthermia with magnetic particles, including targeted treatment, non-invasiveness, minimal downtime, and customization.^{6,7} Apart from magnetic hyperthermia, magnetic nanoparticles serve as contrast agents in MRI, providing higher image contrast. By enhancing the signals of specific tissues, they assist doctors in diagnosing diseases more accurately. In particular, magnetosomes, with their strictly controlled morphology and crystal form, exhibit prominent application advantages in the field of MRI.^{8–10} Furthermore, magnetic nanoparticles can act as drug delivery vehicles, precisely delivering drugs to diseased sites through magnetic guidance, thus minimizing damage to healthy tissues. This precisely targeted delivery approach significantly enhances drug efficacy and reduces side effects.^{11,12} Additionally, magnetic nanoparticles can be used to label specific cells and rapidly separate them through magnetic fields. This is particularly useful in cell therapy and research, facilitating a deeper understanding of cell functions and interactions.¹³ While magnetic hyperthermia has been extensively studied in recent years, resulting in noteworthy progress, its translation to clinical trials remains relatively limited. A significant constraint of magnetic hyperthermia therapy (MHT) lies in its low specific absorption

^aKey Laboratory of Low-grade Energy Utilization Technologies and Systems, Chongqing University, Chongqing 400044, China. E-mail: yunfeiyang@cqu.edu.cn

^bDepartment of Pharmacy, Chongqing University Cancer Hospital, Chongqing 400030, China. E-mail: lilixian@cqu.edu.cn

^cSchool of Physical and Mathematical Sciences, Nanyang Technological University, 21 Nanyang Link, Singapore 637371. E-mail: wensiang@ntu.edu.sg

†Electronic supplementary information (ESI) available: Methods and experimental; chemical materials; preparation of $\text{Mn}_{0.5}\text{Zn}_{0.5}\text{Fe}_2\text{O}_4$ multicore nanoflowers; magneto-photothermal heating measurements; cell culture, biocompatibility, uptake, and cytotoxicity assay; SEM for MZF-NFN and MZF-NFE; XPS for MZF-C, MZF-HS, and MZF-NFN; TEM and EDS for MZF-C, XRD for MZF-C, MZF-HS, and MZF-NFN; FTIR for MZF-HS and MZF-HS-PEG; *H-M* curves for MZF-NFN and MZF-HS; temperature elevation for MZF-HS, MZF-NFN and MZF-NFE; photothermal conversion efficiency; micromagnetic simulation method; mathematical model for simulation; and thermal damage assessment. See DOI: <https://doi.org/10.1039/d4nr00104d>

rate (SAR). Therefore, boosting the SAR of magnetic nanoparticles is a significant modality to gain greater efficiency in hyperthermia. Multicore nanoflowers represent highly efficient nano-heaters in magnetic hyperthermia, exhibiting specific absorption rate (SAR) values that rank among the highest reported for magnetic materials.^{14–16} The elevated SAR observed in magnetic nanoflowers stems from the inherent magnetic exchange couplings present within the core constituents that compose the flower-like assemblies, thereby imparting them with enhanced susceptibility.^{17,18} Furthermore, magnetic nanoflowers exhibit a greater degree of spin surface disorder compared to nanoparticles with single-core morphology, owing to their higher surface/volume ratio.¹⁹ Recent studies have confirmed that the magnetic vortex can effectively enhance the value of the SAR.^{20–23} In a magnetic vortex, the magnetic spins in a ferromagnetic material are arranged in a circular pattern around a central core. This magnetic configuration can be induced in MNPs and has been demonstrated to significantly enhance their heating efficiency in MHT. This enhancement can be attributed to the ever-present perpendicular orientation of the magnetic moment with the magnetic field direction, leading to higher energy dissipation in the form of heat. However, further research studies are needed to fully realize the potential of magnetic vortices in magnetic hyperthermia and to develop more effective methods for inducing and controlling magnetic vortices. Consequently, the multi-vortex states in MNPs are a promising modality to further enhance hyperthermia efficiency. Based on our previous studies, we discovered that the cylindrical geometry of the MNPs facilitates the formation of the triple-vortex state, resulting in a remarkable four-fold increase in heat generation efficiency.^{24,25} The value of the SAR can be greatly enhanced by employing different strategies such as effective anisotropy enhancement,^{26–28} exchange coupled magnets,^{29,30} and magnetic vortex procession.^{17,18} Meanwhile, exploring the promising potential of merging different MNP modalities with hyperthermia therapy to achieve an optimized effect is urgent. Recently, iron oxides have been found to exhibit photothermal effects as well.^{14,31–33} Building upon this understanding, a highly effective strategy involves synergistically combining the effects of magnetic hyperthermia (MHT) and photothermal therapy (PTT) to achieve cumulative heating at a specific site of interest.^{14,15,34–37} The main merit of MHT is that it can be carried out without depth limitation. Nevertheless, MHT generates a significantly lower heating yield per unit mass compared to PTT.^{38–41} The materials used in photothermal therapy are usually non-toxic or of low toxicity, causing minimal side effects to the human body. In addition, due to the high selectivity of photothermal therapy, it can precisely irradiate the tumor area, thereby minimizing damage to surrounding normal tissues and reducing the occurrence of side effects.^{42,43} The combination of magnetic hyperthermia and photothermal therapy presents several advantages over utilizing each approach individually. These include complementary mechanisms, synergistic effects,^{15,32} increased versatility, and non-invasiveness.⁶ Consequently, the combination of dual-

exposure therapies, integrating MHT and PTT, may enable reductions in nanoparticle injection dose and near-infrared (NIR) laser power exposure. Moreover, MNPs are image-trackable, by MRI for the magnetic component, or by photo-acoustic imaging for light absorption.^{44–50} Despite extensive investigations of Fe₃O₄ nanoparticles, their Curie temperature of 585 °C surpasses the desired range (42–47 °C) for efficient heat generation.⁵¹ Prior research has evidenced that manganese-zinc ferrite exhibits a lower Curie temperature, and its magnetic properties can be finely tuned through minor zinc doping.^{52,53} Additionally, manganese-zinc ferrite demonstrates outstanding biocompatibility and remarkable magneto-photothermal properties, rendering it a highly competitive nano-heater for various clinical applications.⁵⁴ By functionalizing manganese-zinc ferrite, beneficial properties for therapy can be achieved. For example, MnZnFe₂O₄ nanoparticles with starch demonstrate good colloidal stability, dispersibility, and heating efficiency.⁵² Core-shell nanoparticles of Zn_xMn_{1-x}Fe₂O₄@SiO₂:zNd³⁺ exhibit synergistic heating effects when exposed simultaneously to an alternating magnetic field and NIR laser.⁵⁵ Additionally, the ferrite materials exhibit a significant Fenton effect, which can catalyze the conversion of H₂O₂ to cytotoxic ·OH in the weakly acidic tumor environment, thus realizing chemodynamic therapy. Moreover, under the action of alternating magnetic fields, ferrite materials generate heat due to hysteresis loss, which can further enhance the Fenton effect.⁵⁶

In this study, Mn_{0.5}Zn_{0.5}Fe₂O₄ structures with ellipsoidal magnetic core nanoflowers (MZF-NFE), cubic Mn_{0.5}Zn_{0.5}Fe₂O₄ (MZF-C), hollow spherical Mn_{0.5}Zn_{0.5}Fe₂O₄ (MZF-HS), and Mn_{0.5}Zn_{0.5}Fe₂O₄ with needle-like magnetic core nanoflowers (MZF-NFN) were synthesized. The heating efficiency of the various structures was experimentally investigated, and the magnetization vortex configurations and reversal behaviors were also systematically studied using micromagnetic simulation. Finally, the magneto-photothermal hyperthermia performance of MZF-NFE was evaluated in MCF-7, BT549, and 4T1 cells under AMF and NIR irradiation.

Results and discussion

The described solvothermal synthesis method is illustrated in Fig. 1a, and the more detailed preparation methods are presented in the Experimental section of the ESI.† In the solvothermal process, sodium acetate is hydrolyzed in solution to provide OH⁻ to precipitate metal cations to form crystal nuclei. The formation of MZF-NFE is dependent on the self-assembled CTAB micelles. The effect of reaction temperature (180 °C, 200 °C, and 220 °C) and the amount of NaAc (10 mmol, 15 mmol, and 20 mmol) on the morphology of MZF was studied. Transmission electron microscopy (TEM) images provide clear evidence of the nanoflower structure observed in the obtained MZF (200 °C and 15 mmol), with an average diameter of 160 nm (Fig. 2b and c). Fig. 1(b) shows the diagram based on MZF-NFE-PEG synergistic MHT/PTT therapy.

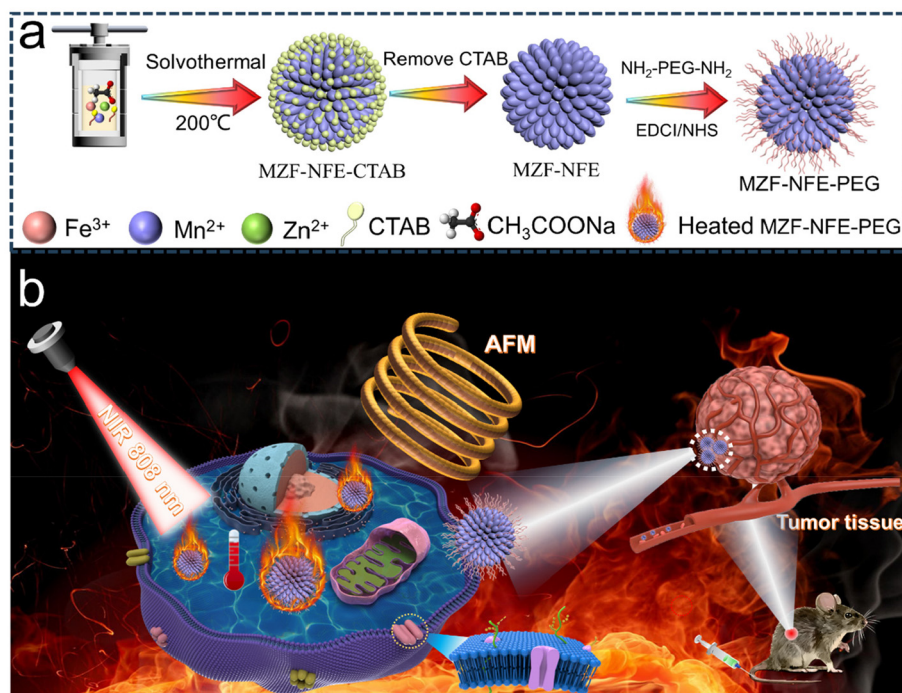


Fig. 1 (a) A schematic that illustrates the synthesis route of MZF–NFE–PEG multicore nanoflowers. (b) Illustration of synergistic MHT/PTT therapy based on MZF–NFE–PEG.

Scanning electron microscopy (SEM) revealed that the as-prepared nanoparticles with an obvious nanoflower structure are well-dispersed (Fig. 2d and e). The SEM images of MZF–NFE that were synthesized at 200 °C with varying amounts of NaAc are shown in Fig. S2a–i.† The results show that the nanoflower structure with needle-like magnetic cores (MZF–NFN) can be obtained by changing the amount of NaAc. The EDS mapping shown in Fig. 2f demonstrates the homogeneous distribution of Mn, Zn, Fe, and O in the obtained MZF–NFE. The interplanar spacing of 0.3 nm, as shown in Fig. 2(g), corresponds to the (220) plane of MZF–NFE, providing confirmation of the spinel structure. The corresponding selected area electron diffraction pattern reveals the presence of weak crystallization in MZF–NFE (Fig. 2h). Moreover, X-ray diffraction (XRD) analysis confirms that the as-prepared sample aligns with the standard peaks (JCPDS no. 74-2403),⁵⁷ as shown in Fig. 2(i).

Fig. 2(j–m) shows the spectra from XPS of Fe 2p, Mn 2p, Mn 3s, and Zn 2p for MZF–NFE, while Fig. S3–S5† show the corresponding spectra for MZF–C, MZF–NFN, and MZF–HS. As shown in Fig. 2(j), the Fe 2p spectrum consists of two primary asymmetric peaks, Fe 2p_{3/2} and Fe 2p_{1/2}, with binding energies of 710.5 and 723.8 eV, respectively. Additionally, the two smaller peaks observed at approximately 718.8 and 731 eV correspond to the satellite peaks of Fe 2p_{3/2} and Fe 2p_{1/2}, respectively.

The results indicate that Fe³⁺ is the sole oxidation state present on the MZF–NFE surface/near-surface. Regarding the Fe 2p_{3/2} peak, three contributions at approximately 709.8, 711,

and 712.3 eV represent distinct circumstances of Fe³⁺ ions. The peaks at 709.8 and 711 eV can be attributed to Fe³⁺ cations with different occupancies (tetrahedral or octahedral) in the spinel ferrite, while the higher binding energy at around 712.3 eV is associated with Fe³⁺ ions bonded with hydroxyl groups.⁵⁸ In high-resolution XPS of Mn 2p, the corresponding Mn 2p_{1/2} and Mn 2p_{3/2} signals are observed at 653 and 641 eV in an ~2 : 1 peak area ratio indicating that Mn is present in an oxidation state (Fig. 2k). Furthermore, two prominent peaks in the Mn 3s spectrum are positioned at 81.2 and 92.6 eV, providing further confirmation of the presence of Mn³⁺ ions. The XPS spectrum of Zn 2p, shown in Fig. 2(m), exhibits two peaks situated at 1021.6 and 1044.6 eV, substantiating the existence of Zn in the corresponding oxidation state.⁵⁹ The FTIR spectra of MZF–NFE–PEG and MZF–NFE are shown in Fig. 2(n). The band observed at 3420 cm⁻¹ is attributed to the O–H stretching mode, corresponding to either free water or absorbed water. Furthermore, the frequency band in the range of 540–560 cm⁻¹ is assigned to the tetrahedral and octahedral M–O stretching bands present in ferrites.⁶⁰ In particular, a new peak was formed at about 890 cm⁻¹ in the MZF–PEG, which belonged to the C–O stretching vibration peak of the ester group of the graft copolymer. The results indicated that PEG was grafted onto the MZF surface. The FTIR spectra of MZF–HS, MZF–HS–PEG and PEG are shown in Fig. S7.†

As observed from the TEM image in Fig. 3a, Mn_{0.5}Zn_{0.5}Fe₂O₄ has a cubic-like structure. EDS mapping is shown in Fig. S6a and S6b.† Fig. 3b displays the TEM image of MZF–NFN with an average size of 250 nm. The MZF–NFN

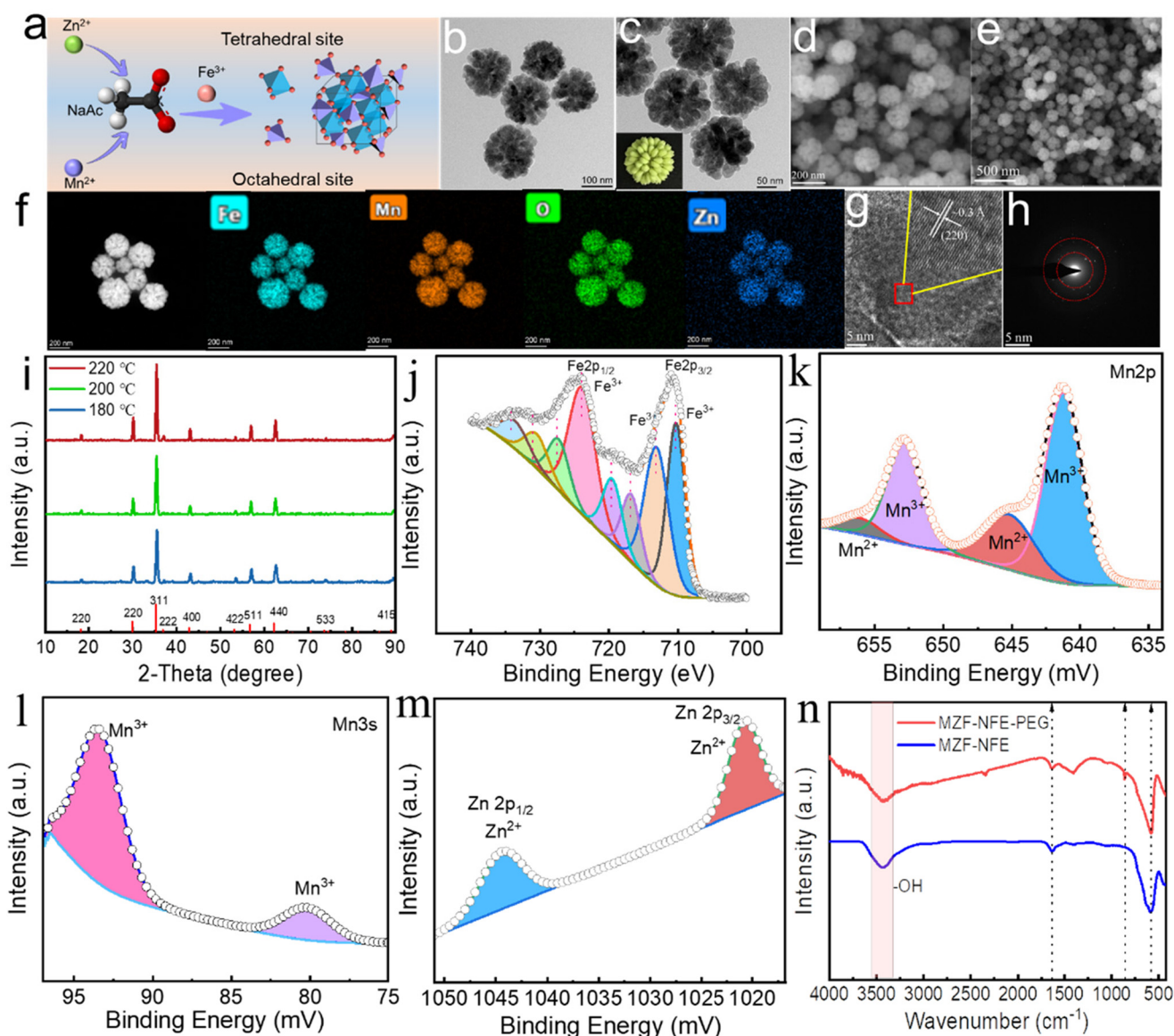


Fig. 2 Morphology and composition characterization of $\text{Mn}_{0.5}\text{Zn}_{0.5}\text{Fe}_2\text{O}_4\text{-PEG}$ (MZF-NFE). (a) Mechanism of spinel structure formation of $\text{Mn}_{0.5}\text{Zn}_{0.5}\text{Fe}_2\text{O}_4$. (b) TEM image of MZF-NFE. (c) TEM image showing the high yield of MZF-NFE-PEG. (d) SEM image of MZF-NFE-PEG. (e) SEM image of well-dispersed MZF-NFE-PEG. (f) EDS mapping shows the elemental compositions of the same structure. (g) Atomic-resolution TEM image of MZF-NFE, and (h) selected area electron diffraction of MZF-NFE. (i) XRD patterns of MZF-NFE-PEG. High-resolution XPS spectra of (j) Fe 2p, (k) Mn 2p, (l) Mn 3s, and (m) Zn 2p. (n) FTIR spectra.

needle-like cores (major axis ≈ 70 nm, and minor axis ≈ 22 nm) are smaller than the MZF-NFE ellipsoidal cores (major axis ≈ 60 nm, and minor axis ≈ 43 nm), as shown in Fig. 3c and d. The EDS mapping shown in Fig. 3e demonstrates the homogeneous distribution of Mn, Zn, Fe, and O in the obtained MZF-NFN. The preparation of hollow spherical $\text{Mn}_{0.5}\text{Zn}_{0.5}\text{Fe}_2\text{O}_4\text{-PEG}$ nanoparticles (Fig. 3f) and the detailed steps are presented in the ESI† (Experimental section). Fig. 3g and h shows the TEM images of MZF-HS nanoparticles, which are hollow spheres with an average diameter of 350 nm. The SEM images clearly show that MZF-HS has a smooth surface and good dispersion (Fig. 3i and j). The TEM-EDS elemental

mapping images suggest the presence of Fe, Mn, Zn, and O components in the nanoparticles (Fig. 3k), and the energy-dispersive X-ray spectroscopy analysis further validates that the as-prepared nanoparticles are composed of pure $\text{Mn}_{0.5}\text{Zn}_{0.5}\text{Fe}_2\text{O}_4$ (Fig. S8a-c†). The N_2 physisorption results of the different shapes of MZF are shown in Fig. 3i. Compared with MZF-NFE, the amount of N_2 adsorbed by the other shapes of MZF decreased significantly. The specific surface area of MZF-NFE was $119 \text{ cm}^3 \text{ g}^{-1}$. The isotherms of MZF-NFE and MZF-NFN exhibited a characteristic type IV feature, indicating the presence of a mesoporous architecture, which enhances their capacity for effective anticarcinogen loading.

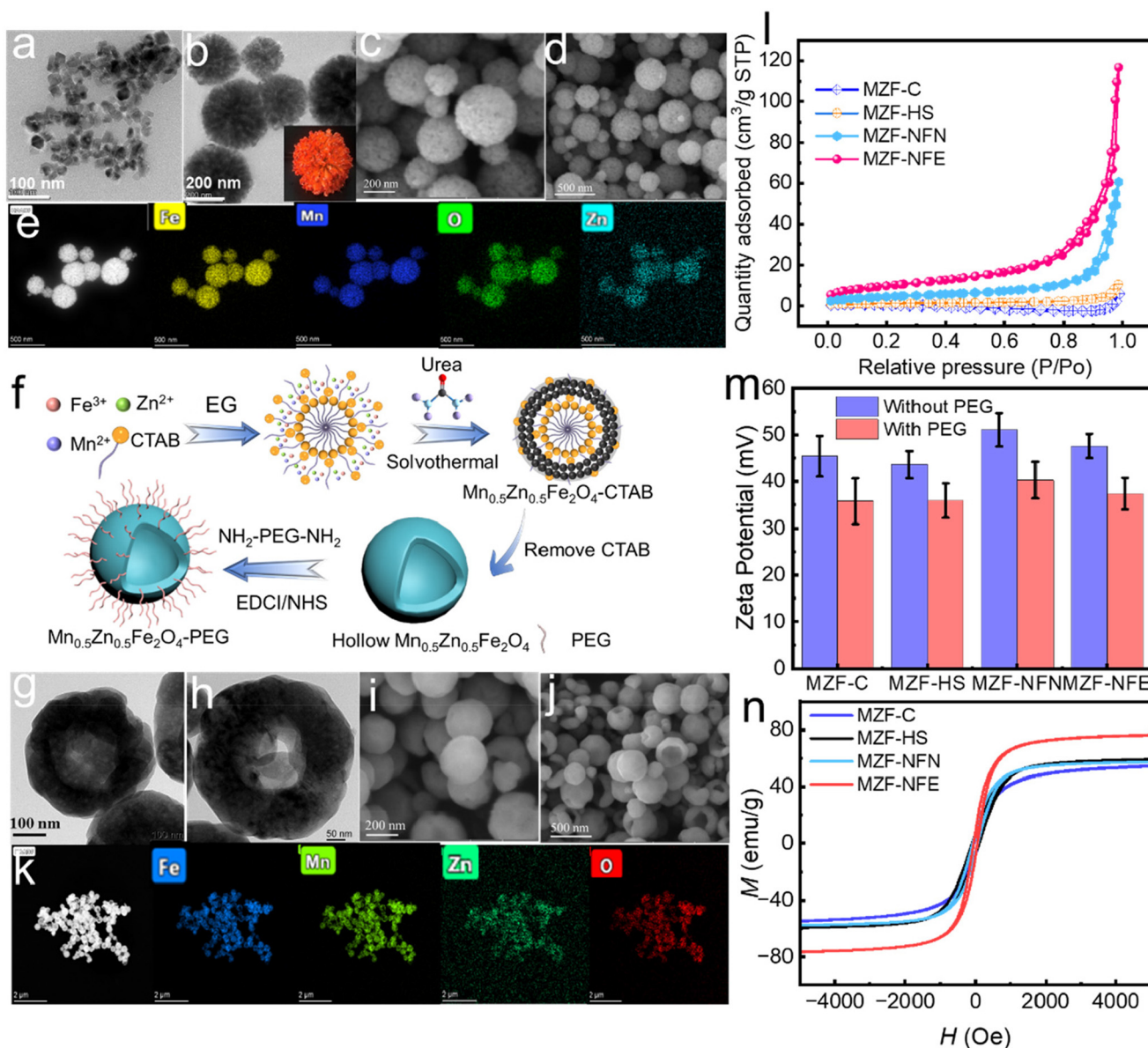


Fig. 3 Morphology and composition characterization of $\text{Mn}_{0.5}\text{Zn}_{0.5}\text{Fe}_2\text{O}_4$. (a) TEM image of cubic $\text{Mn}_{0.5}\text{Zn}_{0.5}\text{Fe}_2\text{O}_4$. (b) TEM image of MZF-NFN. (c) and (d) SEM images of MZF-NFN. (e) TEM-EDS elemental mapping images of an individual MZF-NFN. (f) Illustration of the preparation of hollow spherical $\text{Mn}_{0.5}\text{Zn}_{0.5}\text{Fe}_2\text{O}_4$ -PEG nanoparticles (MZF-HS-PEG). (g) TEM image of MZF-HS nanoparticles. (h) Enhanced TEM image of MZF-HS nanoparticles. (i) and (j) SEM images of MZF-HS nanoparticles. (k) TEM-EDS elemental mapping images of individual MZF-HS nanoparticles. (l) N_2 adsorption-desorption isotherms of the different shapes of MZF. (m) Zeta potential of the four structures with PEG and without PEG. (n) The H - M curves of MZF-C, MZF-HS, MZF-NFE, and MZF-NFN.

The surface charge of $\text{Mn}_{0.5}\text{Zn}_{0.5}\text{Fe}_2\text{O}_4$ nanoparticles with and without PEG was assessed for different shapes by measuring their ζ potential. The magnitude of the ζ potential serves as an indicator of the colloidal system's potential stability. Nanoparticles exhibiting notably positive or negative ζ potential will effectively repel each other, contributing to enhanced dispersion stability.⁵² It was found that all the as-prepared MZF with different shapes exhibited positive ζ potential with magnitudes higher than +37 mV (Fig. 3m). After PEG modification of MZF, the zeta potential value of manganese-zinc ferrite decreased. The main reason is that PEG is a non-ionic

polymer with a large number of ether bonds ($-\text{O}-$) on its molecular chain. When PEG is modified onto the surface of manganese-zinc ferrite, the ether bonds on the PEG molecular chain interact with the surface charges of manganese-zinc ferrite, thereby shielding some of the surface charges, which results in a decrease in the zeta potential value. Additionally, PEG molecules possess excellent hydrophilicity, which enhances the surface hydrophilicity of manganese-zinc ferrite after modification. The increased hydrophilicity reduces the interaction between the surface of manganese-zinc ferrite and water, further decreasing its surface charge density and sub-

sequently lowering the zeta potential value. PEG modification on the surface of manganese–zinc ferrite forms a spatial steric hindrance layer, which prevents direct contact and electrostatic interactions between manganese–zinc ferrite particles. This spatial steric hindrance effect can reduce the surface charge density of manganese–zinc ferrite, thereby decreasing its zeta potential value. The magnetic properties of $\text{Mn}_{0.5}\text{Zn}_{0.5}\text{Fe}_2\text{O}_4$ with the different shapes were investigated using a vibrating sample magnetometer (VSM) at 300 K as demonstrated in Fig. 3n. The saturation magnetization (M_s) values of all samples are between 60.7 and 79.1 emu g^{-1} . MZF–NFN shows the largest M_s value of 79.1 emu g^{-1} , while MZF–C has the

lowest M_s value of 60.7 emu g^{-1} . MZF–HS and MZF–NFN have an almost equal value of 61.7 emu g^{-1} . Additionally, Fig. S9a† shows the M – H curves of MZF–NFN with different solvothermal temperatures (180, 200, and 220 °C). The M_s values are equivalent at different solvothermal temperatures, which indicates that the reaction temperature has little effect on M_s . The M_s value of MZF–NFE increases with the amount of NaAc; however, when the amount of NaAc reaches 20 mmol, the M_s value is equivalent to that for 15 mmol, with both reaching the maximum value of 79.1 emu g^{-1} (Fig. S9b†).

Fig. 4a illustrates the schematic diagram of the photothermal conversion of MZF–NFE. The UV-vis-NIR spectra of MZF–

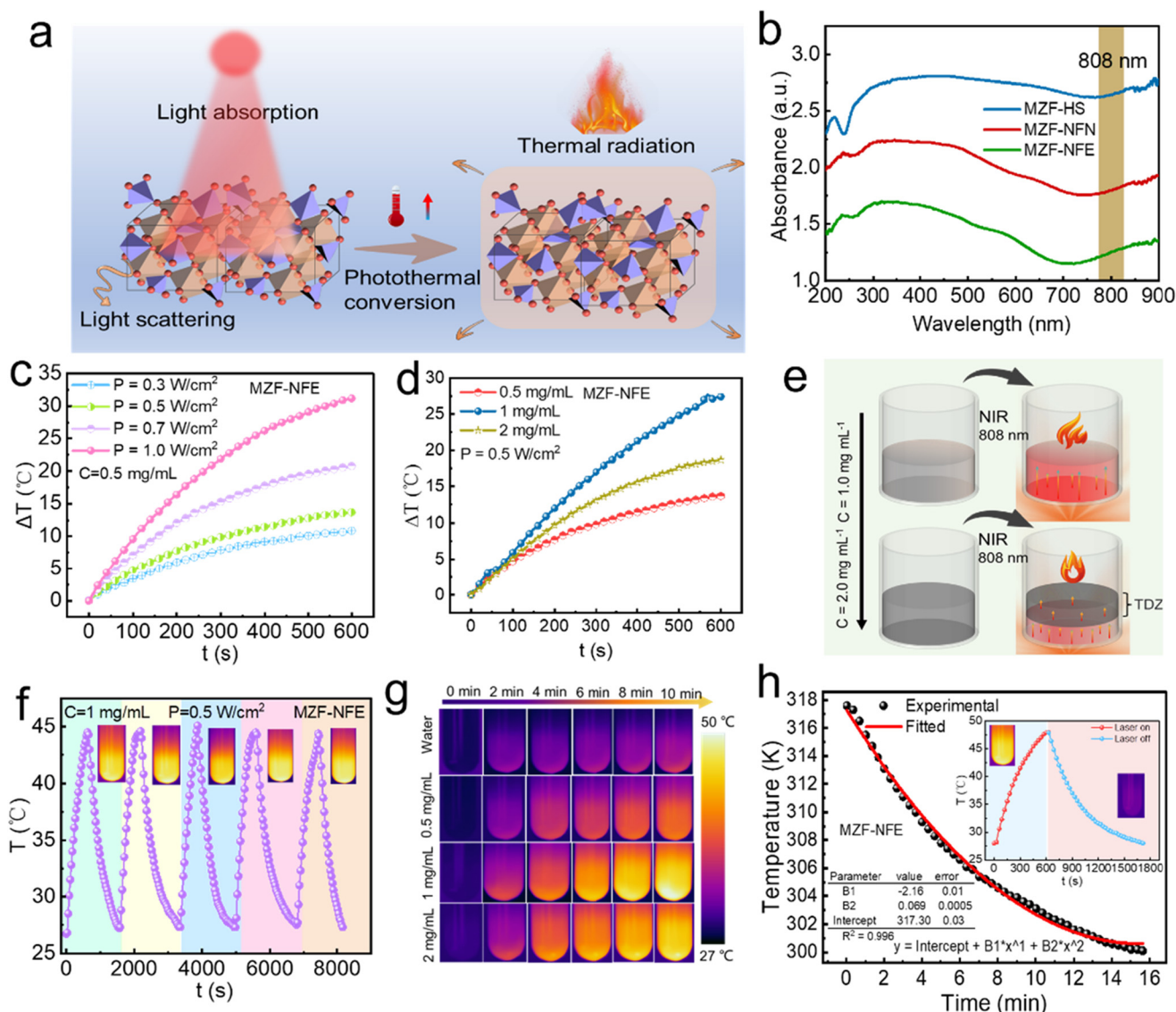


Fig. 4 (a) Schematic diagram of photothermal conversion; (b) UV-vis-NIR spectra of corresponding colloidal dispersions for MZF–HS, MZF–NFE, and MZF–NFN; (c) temperature elevation for an aqueous dispersion of MZF–NFE at a concentration of 0.5 mg mL^{-1} irradiated for 10 min using an 808 nm laser at various power densities. (d) Temperature elevation for MZF–NFE aqueous dispersions at varying concentrations, all irradiated under an 808 nm laser (0.5 W cm^{-2}); (e) heat transfer for MZF–NFE with different concentrations; and (f) the recycling heating–cooling curve of MZF–NFE for five consecutive on/off rounds. (g) Thermal images of MZF–NFE at various concentrations. (h) Experimental and fitted temperature decays of the MZF–NFE solution after the laser was switched off.

HS, MZF–NFN, and MZF–NFE aqueous dispersions are shown in Fig. 4b. Notably, all three nanostructures demonstrated broadband absorption spanning from visible to near-infrared light, with the MZF–HS nanostructure exhibiting particularly high absorbance (2.7) when irradiated with NIR (808 nm). As shown in Fig. 4c, the photothermal conversion performance of MZF–NFE (0.5 mg mL⁻¹) was evaluated at different NIR power densities at room temperature. The ΔT increased by 20.3 °C as the power density increased from 0.3 to 1.0 W cm⁻². More details of the ΔT curves for MZF–NFN, MZF–NFE, and MZF–HS are discussed in Fig. S10a–i.† Besides the NIR power densities, the concentration of the nanoparticles also had a great influence on ΔT (Fig. 4d, Fig. S10i†). At low concentrations, NIR could easily penetrate the MZF–NFE solution, resulting in all the MZF–NFE nanoparticles absorbing NIR. However, when the concentration of MZF–NFE increased, NIR was almost completely absorbed at the bottom of the solution and could not reach the top layer, as shown in Fig. 4e. In addition, the heat generated by the lower MZF–NFE could not be quickly transferred to the top layer as MZF–NFE has low thermal conductivity, resulting in a temperature dead zone (TDZ), which caused a lower overall solution temperature. Photothermal stability is an important characteristic of photothermal agents. There was no noticeable change in the photothermal effect after five cycles of NIR irradiation, indicating that all samples possessed excellent thermal stability and photostability, as shown in Fig. 4f. The more detailed photostability of MZF–NFN and MZF–HS is presented in Fig. S11a and S11b.† Thermal images of MZF–NFE with different concentrations are shown in Fig. 4g. Following the theory proposed by Chen *et al.*⁶¹ (eqn (S1)†), the temperature decay curve for MZF–NFE shown in Fig. 4h was integrated with respect to time (ΔT vs. t) and subsequently fitted; the details of MZF–HS and MZF–NFN are shown in Fig. S12a–c.† The photothermal conversion efficiency (η) rates of MZF–HS, MZF–NFE, and MZF–NFN were calculated to be 24.7%, 20.3%, and 18.6% (Fig. S12d†).

The magnetic heating effects of the different MZF structures with various concentrations were investigated under an AMF. The AMF applied had an amplitude of 60 to 120 Oe with a constant frequency of 300 kHz. An MZF–NFE aqueous solution exhibited a rapid temperature increase, and the ΔT showed a strong dependency on H , with ΔT reaching about 25.3 °C in 10 min with an amplitude of 120 Oe (Fig. 5a). The MZF–NFE aqueous solution had the maximum value of ΔT compared to those of the other three shapes under the same AMF conditions (Fig. S13a–h†). Considering the safe field condition⁶ ($H \times f < 5 \times 10^9$ A m s⁻¹), when comparing the different shapes of MZF, the obtained SAR values under the same AMF parameters indicate the following order in heating performance: $SAR_{\text{MZF-C}} < SAR_{\text{MZF-HS}} < SAR_{\text{MZF-NFN}} < SAR_{\text{MZF-NFE}}$ as shown in Fig. 5b. Details of the SAR values for the different shapes of MZF with varying concentrations can be found in Fig. S14a and 14b.† Notably, the SAR of MZF–NFE was enhanced by close to 7 times that of MZF–C, implying that the shape-controlled synthesis of nanocrystals is vitally important to improve their magnetic hyperthermia performance.

Moreover, as shown in Fig. 5c, the value of the SAR decreases with the concentration of magnetic nanoparticles; further details are presented in Fig. S14c–f.† Furthermore, to quantitatively evaluate the intrinsic material heat induction performance independent of AMF, the ILP values were experimentally determined by measuring the AMF-induced self-heating curves, where $ILP = \frac{SAR}{H^2 f}$. The ILP values are 1.6 nH m² kg⁻¹ for MZF–C and 15.2 nH m² kg⁻¹ for MZF–NFE. As shown in Fig. 5d, the obtained ILP values of the different shapes in water are compared with ILP values of other previously reported magnetic nanoparticles.^{14,33,62–69} MZF–NFE showed the highest value among the magnetic nanoparticles. The value is about 100 times that of commercial iron oxide and is also similar to that of recently reported core/shell exchange-coupled NPs.² The high ILP values of MZF–NFE and MZF–NFN are mainly attributed to magnetic vortices^{21,24} and exchange couplings between the cores.¹⁴ The ILP is linearly correlated with the increase of exchange coupling between the cores.¹⁴ Therefore, the ILP of MZF–NFN should be larger than that of MZF–NFE due to exchange coupling. However, this was not the case, as revealed in Fig. 5d. Instead, the magnetization vortex configuration is another important factor in the heating efficiency of the multicore nanoflowers.^{17,21} Micromagnetic simulations of the MZF–NFE structure show that a multi-vortex configuration is formed at the remanence state. However, no magnetic vortex is formed for MZF–NFN due to the high aspect ratio of the magnetic core; this dependency is in accordance with the results reported by Gao *et al.*⁷⁰ For MZF–NFE, the presence of the exchange coupling and magnetic-vortex configuration simultaneously leads to a higher ILP than that for MZF–NFN. The exceptionally high ILP value of MZF–NFE would potentially enable the nanoparticle to completely kill tumor hyperthermia and extend its effect to magnetic thermoablation for the necrotization of cancer cells.

To investigate heat transfer and ablation inside the tumor tissue loaded with MZF–NFE, a realistic model of a solenoid (Fig. 5e) is employed to evaluate the magnetic field, anticipate the temperature distribution, and estimate the damaged fraction of biological tissue during magnetic hyperthermia treatment. The treatment temperature distribution in the biological tissue of the proposed physical model can be accurately predicted by solving Pennes' bio-heat transfer equation⁷¹ (eqn (S11) and (S12)†). Details of the simulation parameters and model are presented in the Experimental section of the ESI.† The simulated magnetic fields match the measured experimental field, and Fig. 5f illustrates the resulting magnetic field distribution obtained from the simulation. Fig. 5g shows the temperature distribution with varying fields of 60, 80, and 100 Oe. The critical magnetic field of $H = 100$ Oe at $f = 300$ kHz is proposed for optimal temperature at 47 °C for therapy. The extent of tumor tissue damage is significantly influenced by the amplitude of the AMF, as shown in Fig. 5h, where the damaged fraction is more than 0.95 when the amplitude of the magnetic field is at 100 Oe.

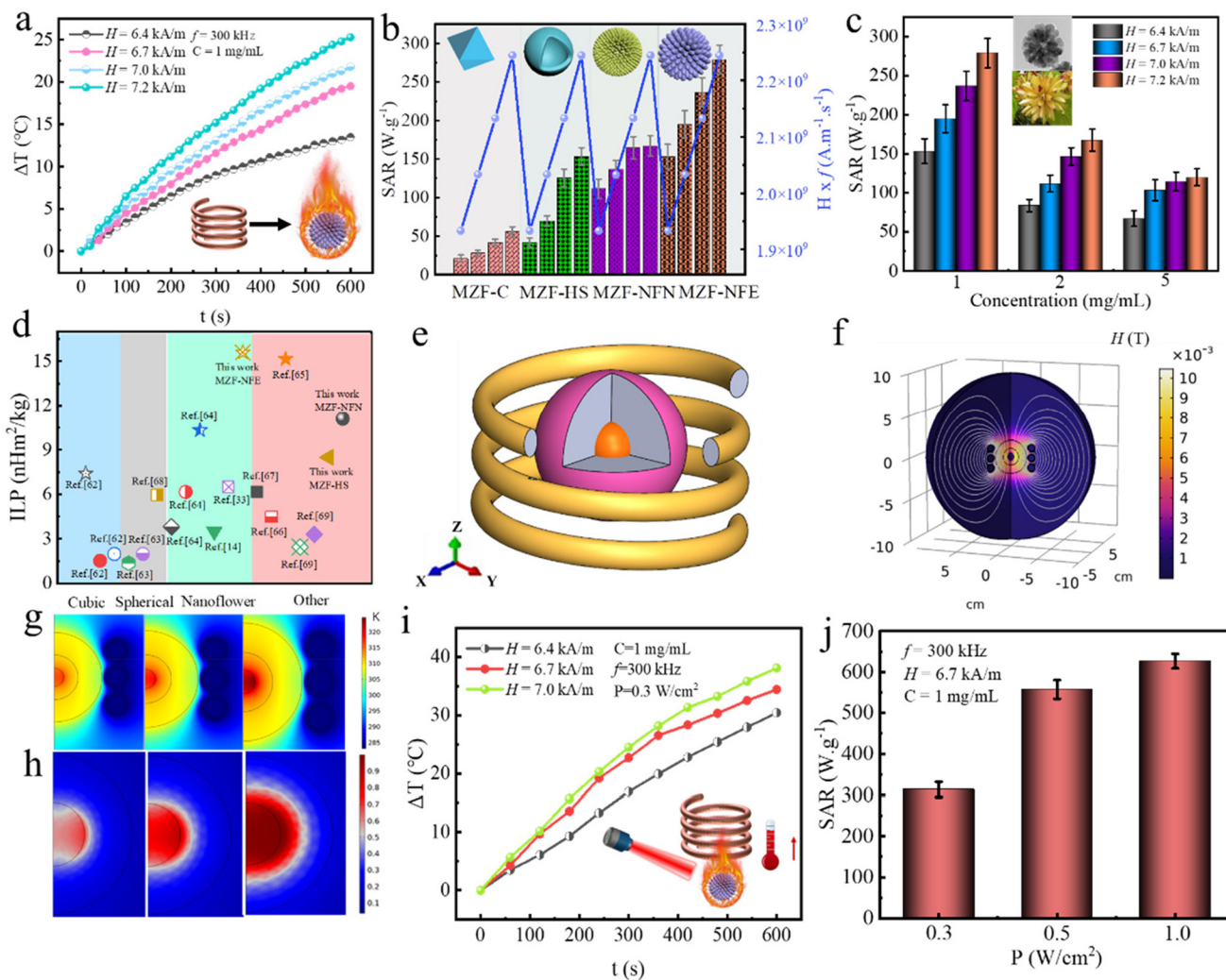


Fig. 5 (a) Heating profiles of the MZF–NFE aqueous solution (1 mg mL^{-1}) under AMF ($f = 300 \text{ kHz}$, $H = 60 \text{ Oe}$ to 120 Oe). (b) The SAR values as a function of $H \times f$ product for MZF (1 mg mL^{-1}) with different shapes. (c) The SAR values of MZF–NFE at different concentrations (1 mg mL^{-1} , 2 mg mL^{-1} , and 5 mg mL^{-1}) under an AC magnetic field ($H = 60$ to 120 Oe) at $f = 300 \text{ kHz}$ excited for 600 s . (d) The heating performance as represented by the ILP values of different MZF shapes. (e) The sectional view presenting the geometrical model for MHT. (f) The magnetic field is generated by the current-carrying solenoid in the y – z plane. (g) Temperature distributions and (h) tissue-damaged fraction inside the tumor for different H values of 60 Oe , 80 Oe , and 100 Oe , respectively. (i) The heating curves for MZF–NFE under various H values (60 Oe to 120 Oe) at $f = 300 \text{ kHz}$, on exposure to an NIR laser at a power density of 0.3 W cm^{-2} . (j) The SAR values of MZF–NFE (1 mg mL^{-1}) as a function of P under an AMF ($H = 80 \text{ Oe}$) at $f = 300 \text{ kHz}$.

As shown in Fig. 5i, the heating capabilities of MZF–NFE triggered by MHT and PTT were studied with different magnetic amplitudes and laser power densities separately, and both parameters can distinctly improve the heating efficiency. As expected, the SAR increases with the NIR and AMF in the dual-exposure mode (Fig. 5j and Fig. S18b†). Under a fixed magnetic field ($H = 60 \text{ Oe}$ and $f = 300 \text{ kHz}$), the specific absorption rate (SAR) significantly increases when a laser is concurrently applied. Consequently, the SAR is significantly higher than it is in MHT and PPT and reaches beyond 600 W g^{-1} in the dual-exposure mode ($P = 0.7 \text{ W cm}^{-2}$ and $H = 60 \text{ Oe}$). Therefore, the dual exposure of AMF and NIR irradiation is very promising in enhancing the heating capacity of MZF–NFE.

The high ILP of the MZF–NFE can originate from the energy of complex magnetization reversal. Micromagnetic simulation using a GPU-accelerated MuMax3 program was carried out to understand the magnetization configurations of the different shapes of MZF.⁷² Typical material parameters of MZF were utilized and are listed in Table S1.† For the cubic-shaped nanoparticles with sizes smaller than 52 nm , the remanent state has a single-domain magnetization configuration. Fig. 6a reveals that there is no vortex from the cubic-shaped nanoparticles. A critical particle size of at least ~ 10 – 30 nm ⁷³ is required for a stable vortex state in MZF–HS. The magnetic configuration for larger-size hollow spheres with a diameter of 300 nm (inner diameter of 100 nm) was simulated and the M –

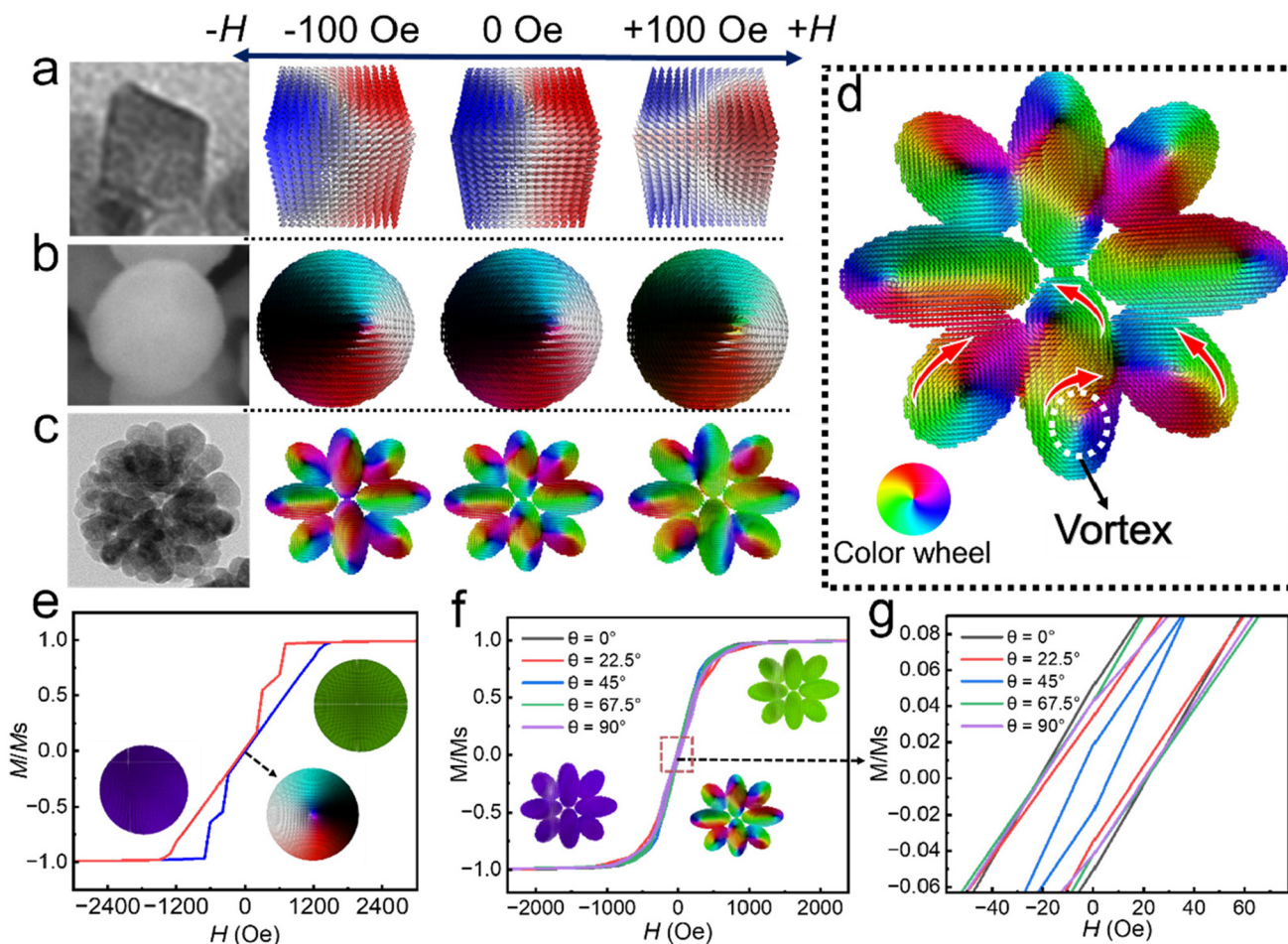


Fig. 6 Micromagnetic simulation of the cyclical variation of magnetic moments from various particle shapes under an alternating magnetic field: (a) cubic, (b) MZF-HS, and (c) MZF-NFE. (d) Simulated magnetization configuration of MZF-NFE at 100 Oe. Simulated normalized hysteresis loops of (e) MZF-HS and (f) MZF-NFE; insets show the magnetization configuration at various magnetic field strengths. (g) Enlarged normalized hysteresis loops of MZF-NFE at low fields.

H curve is shown in Fig. 6e. At a field of $H \sim -800$ Oe, the hollow sphere has a single domain state. Multi-step magnetic state transitions take place when the field decreases as is evident from the sharp magnetization change (Fig. 6e) as well as the differential susceptibility, $\chi = dM/dH$, shown in Fig. S15.† A double-vortex state was observed at $H = -600$ Oe, consisting of a pair of clockwise and counterclockwise vortices and the vortex axis of the two vortices aligns with the magnetic field as shown in Fig. S16.† The magnetic configuration changes into a counterclockwise vortex at $H \sim -300$ Oe. The vortex configuration was retained throughout the magnetic field sweep until $H \sim +600$ Oe, and finally into a single domain state at $+800$ Oe. The multi-step magnetic state transitions observed in Fig. 6e are not present in the experimental equivalent shown in Fig. 3n. This can be attributed to the imperfections and the variations in vortex axes of the nanoparticles used in the VSM measurement. Fig. 6b depicts the magnetic configuration of MZF-HS in the minor magnetic field sweep between -100 Oe and $+100$ Oe; more details can be found in Fig. S17.† These results demonstrate the potential for stable

vortex states to form in submicrometer hollow spherical nanoparticles at low external field. Furthermore, the magnetic vortex configurations and reversal behaviors of MZF-NFE were also studied by varying the nanoparticle orientation angle, θ (0° , 22.5° , 45° , 67.5° , and 90°) between the x -axis and the magnetic field direction, as shown in Fig. S18.† The magnetic ellipsoids of MZF-NFE have an average major axis $a \approx 60$ nm and a minor axis $b \approx 43$ nm. The magnetization configuration in the minor magnetic field sweep between -100 Oe and $+100$ Oe and M - H loops of MZF-NFE by varying θ are presented in Fig. 6c and f, respectively. Fig. 6g shows the M - H loops of MZF-NFE under a low magnetic field; it is observed that MZF-NFE has a lower coercivity, suggesting that the magnetic moment can be reversed at a lower applied magnetic field. More details for switching behaviors at different θ values are shown in Fig. S19.† While MZF-NFE forms the vortex state as the angle θ changes from 0° to 90° , a notable difference in the vortex chirality is evident, as shown in Fig. 6d ($\theta = 0^\circ$). As shown in Fig. S20a and S20b,† when $\theta = 0^\circ$ and 90° , the magnetic cores along the external magnetic field show a pair of

vortices with opposite chirality at the remanent state while only a single vortex was formed in the magnetic cores that deviate from the direction of a magnetic field. However, as shown in Fig. S18,† when $\theta = 22.5^\circ$, $\theta = 45^\circ$ and $\theta = 67.5^\circ$, each magnetic core only forms a single vortex. Details on exchange energy, demagnetization, and Fig. S21a–d† shows the Zeeman energy contributions to the total energy of the MZF–NFE. Additionally, the magnetic coupling between the magnetic cores exhibits significant differences at different orientations in the magnetization processes, as shown in Fig. S22a and b.† Compared with the other structures, MZF–NFE exhibits a multi-vortex configuration, suggesting that it has better heating capacity.

Additionally, MCF-7, 4T1 and BT549 cells are selected to evaluate the intrinsic cytotoxicity of MZF–NFE by MTT. As shown in Fig. 7a, after 48 h of incubation, MZF–NFE demonstrates no significant cytotoxicity against MCF-7, 4T1, and BT549 cells, as evidenced by a cell viability of more than 81%, even at an MZF–NFE concentration of up to $1000 \mu\text{g mL}^{-1}$, highlighting the favorable biosafety profile of MZF–NFE. Furthermore, the cell viability was similar among MCF-7, 4T1

and BT549 cells following treatment with the same concentration of MZF–NFE.

Combining PTT and MHT can effectively enhance the heating effect, hence investigations on their phototherapeutic and magnetic hyperthermia therapy effect on MCF-7, 4T1, and BT549 cells *in vitro* were carried out. As shown in Fig. 7b, upon exposure to an AMF ($f = 300 \text{ kHz}$, $H = 80 \text{ Oe}$) and irradiation with NIR (0.5 W cm^{-2}) separately, the cell viability is maintained at a high level (17.6% for AFM, 12.4% for NIR). However, upon exposure to AFM and NIR irradiation, a significant increase in cell death was observed, with over 95.7% of cell death occurring at an MZF–NFE concentration of 1.0 mg mL^{-1} . These results indicate that MZF–NFE is an excellent system for synergistic MHT/PTT. Moreover, to assess cell viability, a fluorescent LIVE/DEAD assay was performed, and the results are shown in Fig. 7c. In the control group, almost no dead cells were observed. In the magnetic hyperthermia (MHT) group, approximately 60% of the cells died, while the photothermal therapy (PTT) group exhibited around 65% cell death. Remarkably, nearly all cells died in the dual-exposure group. Consistent with the above-mentioned findings, these

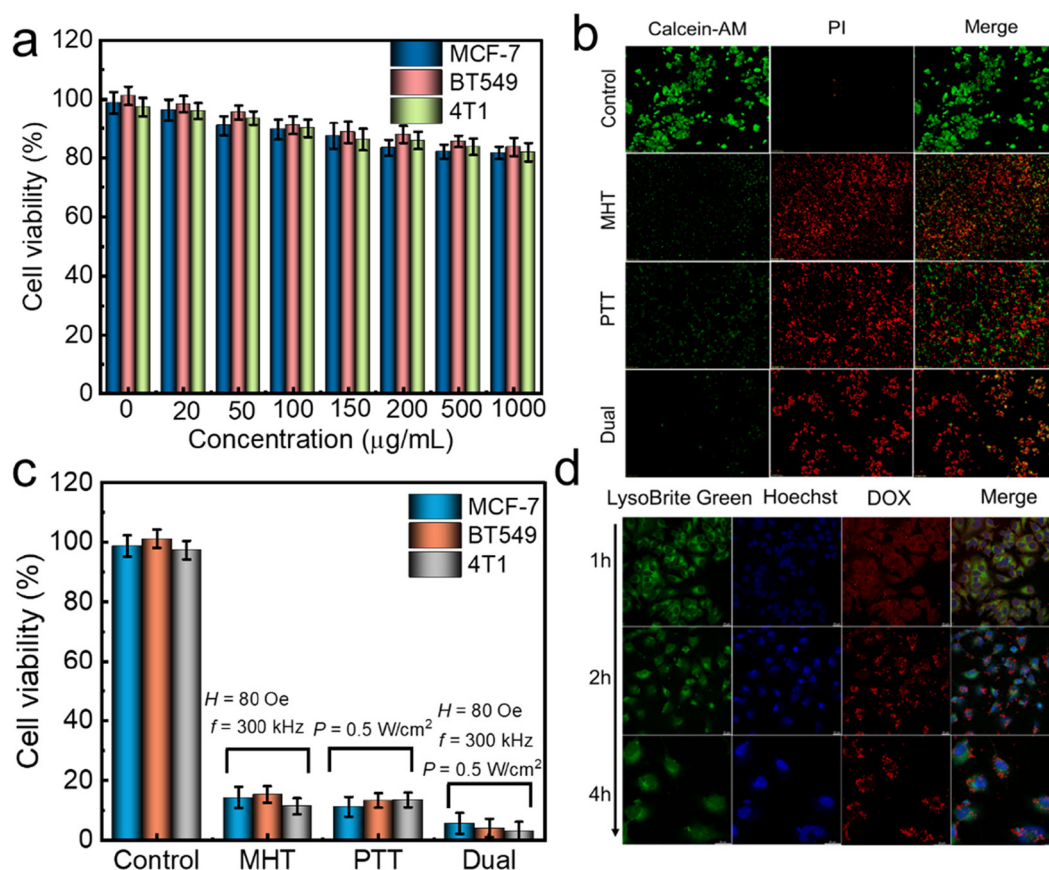


Fig. 7 (a) Confocal images of calcein–AM (green, live cells) and PI (red, dead cells) dye-contained cells incubated with MZF–NFE (1 mg mL^{-1}) and treated with MHT (300 kHz , 80 Oe), PTT (0.5 W cm^{-2}) and dual exposure for 10 min. (b) Cell viability of BT549, 4T1 and MCF-7 cells incubated with MZF–NFE at various concentrations for 24 h. (c) Cell viability of BT549, 4T1 and MCF-7 cells incubated with MZF–NFE in the presence of AMF (300 kHz , 80 Oe), NIR laser, and dual exposure for 10 min. (d) Confocal microscope images of cellular uptake of MZF–NFE in BT549 cells after 1, 2, and 4 h.

observations reveal the exceptional synergistic effects of MZF-NFE in magnetic hyperthermia therapy (MHT) and photothermal therapy (PTT) at the cellular level. To monitor the uptake behavior of MZF-NFE, fluorescence images were obtained using confocal laser scanning microscopy. Cell nuclei were stained with Hoechst, producing blue fluorescence under illumination with a 405 nm laser. On the other hand, MZF-NFE/DOX emitted red light under the excitation of a 488 nm laser. Additionally, lysosomes were stained with LysoBrite green, generating green fluorescence when exposed to a 500 nm light source. As shown in Fig. 7d and Fig. S19,† BT549 and MCF-7 cells incubated with MZF-NFE/DOX exhibit distinctly red fluorescence signals in the lysosome and colocalization with LysoBrite green, indicating that MZF-NFE/DOX was taken up into the BT549 cells *via* an endolysosomal pathway. Notably, the cells incubated with MZF-NFE/DOX exhibited slightly weaker red fluorescence signals after 1 h, but only small amounts of MZF-NFE/DOX were found inside the cells, which can be attributed to the free DOX small molecules being taken up into cells by passive transport as the main fashion.⁷⁴ In contrast, stronger red fluorescence signals and more MZF-NFE/DOX were found inside the lysosome after incubation for 4 h. The primary reason is that nanoscale biomaterials typically depend on endocytic pathways for cell entry, which is energy-dependent and relatively slow.⁷⁵

Conclusions

In conclusion, we have successfully synthesized $\text{Mn}_{0.5}\text{Zn}_{0.5}\text{Fe}_2\text{O}_4$ nanoflowers with ellipsoidal and needle-like magnetic cores, cubic $\text{Mn}_{0.5}\text{Zn}_{0.5}\text{Fe}_2\text{O}_4$, and hollow spherical $\text{Mn}_{0.5}\text{Zn}_{0.5}\text{Fe}_2\text{O}_4$ *via* a solvothermal method, and a systematic investigation was conducted to assess their photothermal properties and magnetization vortex configurations. The synthesized MZF-HS nanoparticles have a maximum photothermal conversion efficiency of 24.7%. Additionally, MZF-NFE has the highest ILP value of $15.3 \text{ nH m}^2 \text{ kg}^{-1}$, which is attributed to the formation of multiple magnetic vortices. *In vitro* experiments demonstrated that cell viability is at 17.6% for AFM and 12.4% for NIR. However, with the proposed dual-exposure therapy, the cell viability decreased significantly to 4.3% at an MZF-NFE concentration of 1.0 mg mL^{-1} . Therefore, this work demonstrates that MZF-NFE has the potential for efficient cancer hyperthermia therapy using the dual-exposure magneto-photothermal approach.

Conflicts of interest

There are no conflicts to declare.

Acknowledgements

The authors gratefully acknowledge financial support from the Fundamental Research Funds for the Central Universities (2019CDYGYB022), and the Natural Science Foundation of

Chongqing (cstc2021jcyj-msxmX0448). This study was also supported by the projects of the Chongqing Clinical Pharmacy Key Specialties Construction Project and the Young and Middle-aged Leading Medical Talents of the Chongqing Health Commission.

References

- C. Chen, P. Wang, H. Chen, X. Wang, M. N. Halgamuge, C. Chen and T. Song, *ACS Appl. Mater. Interfaces*, 2022, **14**, 14049–14058.
- X. Liu, Y. Zhang, Y. Wang, W. Zhu, G. Li, X. Ma, Y. Zhang, S. Chen, S. Tiwari, K. Shi, S. Zhang, H. M. Fan, Y. X. Zhao and X. J. Liang, *Theranostics*, 2020, **10**, 3793–3815.
- C. R. Kalaiselvan, S. S. Laha, S. B. Somvanshi, T. A. Tabish, N. D. Thorat and N. K. Sahu, *Coord. Chem. Rev.*, 2022, **473**, 214809.
- E. Myrovali, N. Maniotis, T. Samaras and M. Angelakeris, *Nanoscale Adv.*, 2020, **2**, 408–416.
- E. P. McKiernan, C. Moloney, T. R. Chaudhuri, S. Clerkin, K. Behan, R. M. Straubinger, J. Crean and D. F. Brougham, *Acta Biomater.*, 2022, **152**, 393–405.
- H. Gavilan, S. K. Avugadda, T. Fernandez-Cabada, N. Soni, M. Cassani, B. T. Mai, R. Chantrell and T. Pellegrino, *Chem. Soc. Rev.*, 2021, **50**, 11614–11667.
- J. Pan, Y. Xu, Q. Wu, P. Hu and J. Shi, *J. Am. Chem. Soc.*, 2021, **143**, 8116–8128.
- J. Yao, F. Zheng, F. Yang, C. Yao, J. Xing, Z. Li, S. Sun, J. Chen, X. Xu, Y. Cao, N. Hampp and A. Wu, *Biomater. Sci.*, 2021, **9**, 7591–7602.
- Y. L. Balachandran, W. Wang, H. Yang, H. Tong, L. Wang, F. Liu, H. Chen, K. Zhong, Y. Liu and X. Jiang, *ACS Nano*, 2022, **16**, 5647–5659.
- F. M. E. Segers, A. V. Ruder, M. M. Westra, T. Lammers, S. M. Dadfar, K. Roemhild, T. S. Lam, M. E. Kooi, K. Cleutjens, F. K. Verheyen, G. W. H. Schurink, G. R. Haenen, T. J. C. van Berkel, I. Bot, B. Halvorsen, J. C. Sluimer and E. A. L. Biessen, *Cardiovasc. Res.*, 2023, **118**, 3346–3359.
- A. C. C. Sousa, A. I. B. Romo, R. R. Almeida, A. C. C. Silva, L. M. U. Fechine, D. H. A. Brito, R. M. Freire, D. P. Pinheiro, L. M. R. Silva, O. D. L. Pessoa, J. C. Denardin, C. Pessoa and N. M. P. S. Ricardo, *Carbohydr. Polym.*, 2021, **264**, 118017.
- X. Deng, Y. Su, M. Xu, D. Gong, J. Cai, M. Akhter, K. Chen, S. Li, J. Pan, C. Gao, D. Li, W. Zhang and W. Xu, *Biosens. Bioelectron.*, 2023, **222**, 114960.
- Q. Y. Wong, N. Liu, C.-G. Koh, H.-Y. Li and W. S. Lew, *Microfluid. Nanofluid.*, 2016, **20**, 139.
- E. Bertuit, E. Benassai, G. Meriguet, J. M. Greneche, B. Baptiste, S. Neveu, C. Wilhelm and A. Abou-Hassan, *ACS Nano*, 2022, **16**(1), 271–284.
- A. Curcio, A. K. A. Silva, S. Cabana, A. Espinosa, B. Baptiste, N. Menguy, C. Wilhelm and A. Abou-Hassan, *Theranostics*, 2019, **9**, 1288–1302.

- 16 R. Das, N. Rinaldi-Montes, J. Alonso, Z. Amghouz, E. Garaio, J. A. Garcia, P. Gorria, J. A. Blanco, M. H. Phan and H. Srikanth, *ACS Appl. Mater. Interfaces*, 2016, **8**, 25162–25169.
- 17 X. Liu, J. Zheng, W. Sun, X. Zhao, Y. Li, N. Gong, Y. Wang, X. Ma, T. Zhang, L. Y. Zhao, Y. Hou, Z. Wu, Y. Du, H. Fan, J. Tian and X. J. Liang, *ACS Nano*, 2019, **13**, 8811–8825.
- 18 M.-K. Kim, J. Sim, J.-H. Lee and S.-K. Kim, *J. Appl. Phys.*, 2019, **125**, 063901.
- 19 D. Aurelio and J. Vejpravova, *Nanomaterials*, 2020, **10**, 1149.
- 20 R. Das, C. Witanachchi, Z. Nemati, V. Kalappattil, I. Rodrigo, J. Á. García, E. Garaio, J. Alonso, V. D. Lam, A.-T. Le, M.-H. Phan and H. Srikanth, *Appl. Sci.*, 2020, **10**(3), 787.
- 21 X. L. Liu, Y. Yang, C. T. Ng, L. Y. Zhao, Y. Zhang, B. H. Bay, H. M. Fan and J. Ding, *Adv. Mater.*, 2015, **27**, 1939–1944.
- 22 N. A. Usov, M. S. Nesmeyanov and V. P. Tarasov, *Sci. Rep.*, 2018, **8**, 1224.
- 23 J. Bao, S. Guo, X. Zu, Y. Zhuang, D. Fan, Y. Zhang, Y. Shi, Z. Ji, J. Cheng and X. Pang, *Front. Bioeng. Biotechnol.*, 2021, **9**, 721617.
- 24 W. L. Gan, M. Chandra Sekhar, D. W. Wong, I. Purnama, S. Y. Chiam, L. M. Wong and W. S. Lew, *Appl. Phys. Lett.*, 2014, **105**, 152405.
- 25 W. Wong, W. L. Gan, Y. K. Teo and W. S. Lew, *Nanoscale Res. Lett.*, 2019, **14**, 376.
- 26 S. Geng, H. Yang, X. Ren, Y. Liu, S. He, J. Zhou, N. Su, Y. Li, C. Xu, X. Zhang and Z. Cheng, *Chem.–Asian J.*, 2016, **11**, 2996–3000.
- 27 H. Mamiya, H. Fukumoto, J. L. Cuya Huaman, K. Suzuki, H. Miyamura and J. Balachandran, *ACS Nano*, 2020, **14**, 8421–8432.
- 28 P. Garcia-Acevedo, M. A. Gonzalez-Gomez, A. Arnosa-Prieto, L. de Castro-Alves, Y. Pineiro and J. Rivas, *Adv. Sci.*, 2022, e2203397, DOI: [10.1002/advs.202203397](https://doi.org/10.1002/advs.202203397).
- 29 J. Robles, R. Das, M. Glassell, M. H. Phan and H. Srikanth, *AIP Adv.*, 2018, **8**, 056719.
- 30 K. Simeonidis, C. Martinez-Boubeta, D. Serantes, S. Ruta, O. Chubykalo-Fesenko, R. Chantrell, J. Oro-Sole, L. Balcells, A. S. Kamzin, R. A. Nazipov, A. Makridis and M. Angelakeris, *ACS Appl. Nano Mater.*, 2020, **3**, 4465–4476.
- 31 X. Yu, T. Yang, R. Liu, D. Wu, D. Tian, T. Zhou, H. Yan, S. He and H. Zeng, *Small*, 2022, **18**, e2205037.
- 32 P. Pan, Y. Lin, Z. Gan, X. Luo, W. Zhou and N. Zhang, *J. Appl. Phys.*, 2018, **123**, 115115.
- 33 S. K. Shaw, J. Kailashiya, A. Gangwar, S. K. Alla, S. K. Gupta, C. L. Prajapat, S. S. Meena, D. Dash, P. Maiti and N. K. Prasad, *Appl. Surf. Sci.*, 2021, **560**, 150025.
- 34 S. Fiorito, N. Soni, N. Silvestri, R. Brescia, H. Gavilan, J. S. Conteh, B. T. Mai and T. Pellegrino, *Small*, 2022, **18**, e2200174.
- 35 M. Rincon-Iglesias, I. Rodrigo, L. B. Berganza, E. S. A. Serea, F. Plazaola, S. Lanceros-Mendez, E. Lizundia and J. Reguera, *ACS Appl. Mater. Interfaces*, 2022, **14**, 7130–7140.
- 36 S. K. Sharma, N. Shrivastava, F. Rossi, L. D. Tung and N. T. K. Thanh, *Nano Today*, 2019, **29**, 100795.
- 37 L. Liu, H. Zhang, L. Peng, D. Wang, Y. Zhang, B. Yan, J. Xie, S. Xing, F. Peng and X. Liu, *Acta Biomater.*, 2023, **158**, 660–672.
- 38 H. Arami, S. Kananian, L. Khalifehzadeh, C. B. Patel, E. Chang, Y. Tanabe, Y. Zeng, S. J. Madsen, M. J. Mandella, A. Natarajan, E. E. Peterson, R. Sinclair, A. S. Y. Poon and S. S. Gambhir, *Nat. Nanotechnol.*, 2022, **17**, 1015–1022.
- 39 J. Chen, M. Gong, Y. Fan, J. Feng, L. Han, H. L. Xin, M. Cao, Q. Zhang, D. Zhang, D. Lei and Y. Yin, *ACS Nano*, 2022, **16**, 910–920.
- 40 N. Yang, Y. Kang, Y. Cong, X. Wang, C. Yao, S. Wang and L. Li, *Adv. Mater.*, 2022, e2208349, DOI: [10.1002/adma.202208349](https://doi.org/10.1002/adma.202208349).
- 41 Y. Zhang, Z. Guo, H. Zhu, W. Xing, P. Tao, W. Shang, B. Fu, C. Song, Y. Hong, M. D. Dickey and T. Deng, *J. Am. Chem. Soc.*, 2022, **144**, 6779–6790.
- 42 R. Zhao, Y. Zhu, L. Feng, B. Liu, Y. Hu, H. Zhu, Z. Zhao, H. Ding, S. Gai and P. Yang, *Adv. Mater.*, 2024, **36**, e2307115.
- 43 F. Gao, Y. Miao, H. Ma, T. Zhang, H. Fan and L. Zhao, *Nanoscale*, 2021, **13**, 14960–14972.
- 44 F. M. E. Segers, A. V. Ruder, M. M. Westra, T. Lammers, S. M. Dadfar, K. Roemhild, T. S. Lam, M. Eline Kooi, K. Cleutjens, F. K. Verheyen, G. W. H. Schurink, G. R. Haenen, T. J. C. van Berkel, I. Bot, B. Halvorsen, J. C. Sluimer and E. A. L. Biessen, *Cardiovasc. Res.*, 2022, **118**, 3346–3359.
- 45 K. X. Vazquez-Prada, S. S. Moonshi, Y. Wu, F. Akther, B. W. C. Tse, K. A. Sokolowski, K. Peter, X. Wang, G. Xu and H. T. Ta, *Small*, 2023, e2205744, DOI: [10.1002/smll.202205744](https://doi.org/10.1002/smll.202205744).
- 46 B. Yin, W. K. H. Ho, X. Xia, C. K. W. Chan, Q. Zhang, Y. M. Ng, C. Y. K. Lam, J. C. W. Cheung, J. Wang, M. Yang and S. H. D. Wong, *Small*, 2023, e2206762, DOI: [10.1002/smll.202206762](https://doi.org/10.1002/smll.202206762).
- 47 A. S. C. Goncalves, C. F. Rodrigues, A. F. Moreira and I. J. Correia, *Acta Biomater.*, 2020, **116**, 105–137.
- 48 Z. W. Lim, V. B. Varma, R. V. Ramanujan and A. Miserez, *Acta Biomater.*, 2020, **110**, 221–230.
- 49 C. Zhang, J. Wu, W. Liu, W. Zhang, C. S. Lee and P. Wang, *Acta Biomater.*, 2023, **159**, 247–258.
- 50 Y. Wang, A. Barhoumi, R. Tong, W. Wang, T. Ji, X. Deng, L. Li, S. A. Lyon, G. Reznor, D. Zurakowski and D. S. Kohane, *Acta Biomater.*, 2018, **72**, 287–294.
- 51 J. Xie, C. Yan, Y. Yan, L. Chen, L. Song, F. Zang, Y. An, G. Teng, N. Gu and Y. Zhang, *Nanoscale*, 2016, **8**, 16902–16915.
- 52 S. V. Jadhav, B. M. Kim, H. Y. Lee, I. C. Im, A. A. Rokade, S. S. Park, M. P. Patil, G. D. Kim, Y. S. Yu and S. H. Lee, *J. Alloys Compd.*, 2018, **745**, 282–291.
- 53 N. Kaur and B. Chudasama, *J. Magn. Magn. Mater.*, 2018, **465**, 164–168.
- 54 T. Kondo, K. Mori, M. Hachisu, T. Yamazaki, D. Okamoto, M. Watanabe, K. Gonda, H. Tada, Y. Hamada, M. Takano, N. Ohuchi and Y. Ichianagi, *J. Appl. Phys.*, 2015, **117**, 17D157.
- 55 M. Vinícius-Araújo, N. Shrivastava, A. A. Sousa-Junior, S. A. Mendanha, R. C. D. Santana and A. F. Bakuzis, *ACS Appl. Nano Mater.*, 2021, **4**, 2190–2210.

- 56 J. Shen, T. W. Rees, Z. Zhou, S. Yang, L. Ji and H. Chao, *Biomaterials*, 2020, **251**, 120079.
- 57 G. Padmapriya, A. Manikandan, V. Krishnasamy, S. K. Jaganathan and S. A. Antony, *J. Supercond. Novel Magn.*, 2016, **29**, 2141–2149.
- 58 M. Li, H. Fang, H. Li, Y. Zhao, T. Li, H. Pang, J. Tang and X. Liu, *J. Supercond. Novel Magn.*, 2017, **30**, 2275–2281.
- 59 T. Nie, S. Cao, Y. Wang, Z. Ji, Z. Bai, J. Yan and X. Yan, *Energy Technol.*, 2021, **9**, 2100249.
- 60 K. Shen, Y. Yan, W. Gao, H. Li, W. Chen, Z. He and L. Li, *J. Alloys Compd.*, 2022, **926**, 166806.
- 61 H. Chen, L. Shao, T. Ming, Z. Sun, C. Zhao, B. Yang and J. Wang, *Small*, 2010, **6**, 2272–2280.
- 62 P. Guardia, A. Riedinger, S. Nitti, G. Pugliese, S. Marras, A. Genovese, M. E. Materia, C. Lefevre, L. Manna and T. Pellegrino, *J. Mater. Chem. B*, 2014, **2**, 4426–4434.
- 63 M. Marciello, J. Pellico, I. Fernandez-Barahona, F. Herranz, J. Ruiz-Cabello and M. Filice, *Interface Focus*, 2016, **6**, 20160055.
- 64 P. de la Presa, Y. Luengo, M. Multigner, R. Costo, M. P. Morales, G. Rivero and A. Hernando, *J. Phys. Chem. C*, 2012, **116**, 25602–25610.
- 65 P. Hugounenq, M. Levy, D. Alloyeau, L. Lartigue, E. Dubois, V. Cabuil, C. Ricolleau, S. Roux, C. Wilhelm, F. Gazeau and R. Bazzi, *J. Phys. Chem. C*, 2012, **116**, 15702–15712.
- 66 J. H. Lee, J. T. Jang, J. S. Choi, S. H. Moon, S. H. Noh, J. W. Kim, J. G. Kim, I. S. Kim, K. I. Park and J. Cheon, *Nanotechnol.*, 2011, **6**, 418–422.
- 67 Y. Yang, X. Liu, Y. Lv, T. S. Herng, X. Xu, W. Xia, T. Zhang, J. Fang, W. Xiao and J. Ding, *Adv. Funct. Mater.*, 2015, **25**, 812–820.
- 68 A. Plan Sangnier, S. Preveral, A. Curcio, Amanda K. A. Silva, C. T. Lefevre, D. Pignol, Y. Lalatonne and C. Wilhelm, *J. Controlled Release*, 2018, **279**, 271–281.
- 69 G. Niraula, J. A. H. Coaquira, G. Zoppellaro, B. M. G. Villar, F. Garcia, A. F. Bakuzis, J. P. F. Longo, M. C. Rodrigues, D. Muraca, A. I. Ayesh, F. S. M. Sinfrônio, A. S. de Menezes, G. F. Goya and S. K. Sharma, *ACS Appl. Nano Mater.*, 2021, **4**, 3148–3158.
- 70 H. Gao, T. Zhang, Y. Zhang, Y. Chen, B. Liu, J. Wu, X. Liu, Y. Li, M. Peng, Y. Zhang, G. Xie, F. Zhao and H. M. Fan, *J. Mater. Chem. B*, 2020, **8**, 515–522.
- 71 Y. Tang, R. C. C. Flesch, T. Jin and M. He, *Int. J. Heat Mass Transfer*, 2021, **178**, 121609.
- 72 A. Vansteenkiste, J. Leliaert, M. Dvornik, M. Helsen, F. Garcia-Sanchez and B. Van Waeyenberge, *AIP Adv.*, 2014, **4**, 107133.
- 73 N. Hirano, S. Kobayashi, E. Nomura, M. Chiba, H. Kasai, Z. Akase, T. Akashi, A. Sugawara and H. Shinada, *Appl. Phys. Lett.*, 2021, **119**, 132401.
- 74 Y. Wang, S. Luo, Y. Wu, P. Tang, J. Liu, Z. Liu, S. Shen, H. Ren and D. Wu, *ACS Nano*, 2020, **14**, 17046–17062.
- 75 N. Liu, L. Wu, W. Zuo, Q. Lin, J. Liu, Q. Jin, Z. Xiao, L. Chen, Y. Zhao, J. Zhou and X. Zhu, *ACS Appl. Mater. Interfaces*, 2022, **14**, 29668–29678.